Richard Jefferson-Loveday

First Last

ASME Paper Title: Simulation of a Simplified Aeroengine Bearing Chamber Using a Fully Coupled Two-Way Eulerian Thin Film /Discrete Phase Approach Part I: Film Behavior Near the Bearing

Authors: Andrew Nicoli, Kathy Johnson, Richard Jefferson-Loveday

ASME Journal Title: Journal of Engineering for Gas Turbines and Power

Volume/Issue 143/10 Date of Publication (VOR* Online) September 2021

ASME Digital Collection URL: https://asmedigitalcollection.asme.org/gasturbinespower/article-abstract/143/10/101015/1111623/Simulation-of-a-Simplified-Aeroengine-Bearing?redirectedFrom=fulltext

DOI: 10.1115/1.4051560

Journal of Engineering for Gas Turbines and Power

GTP-21-1138

SIMULATION OF A SIMPLIFIED AEROENGINE BEARING CHAMBER USING A FULLY COUPLED TWO-WAY EULERIAN THIN FILM/DISCRETE PHASE APPROACH PART I: FILM BEHAVIOUR NEAR THE BEARING

Andrew Nicoli
Andrew.Nicoli1@nottingham.ac.uk
G2TRC, The University of Nottingham, UK

Kathy Johnson
Kathy.Johnson@nottingham.ac.uk
G2TRC, The University of Nottingham, UK

Richard Jefferson-Loveday
Richard.Jefferson-Loveday@nottingham.ac.uk
G2TRC, The University of Nottingham, UK

ABSTRACT

Previous work at the Gas Turbine and Transmissions Research Centre (G2TRC) has highlighted the need for an adequate computational model which can appropriately model the oil shedding behaviour from bearings. Oil can breakup forming droplets and ligaments, subsequently forming thin and thick films driven by both gravity and shear. Our previously published work using OpenFOAM successfully coupled the Eulerian thin film model (ETFM) with the discrete phase model (DPM) [1]. In this paper, the previously developed ETFM-DPM capability is, for the first time, extended to an aeroengine representative bearing chamber configuration. The configuration matches that of a simplified aeroengine bearing chamber that has been investigated by researchers at the Gas Turbine and Transmissions Research Centre (G2TRC).

Numerical investigations are conducted for three different shaft speeds namely 5,000, 7,000 and 12,000 rpm, at two different oil flow rates: 7.3 l/min and 5.2 l/min. CFD results are validated against existing experimental data for the two lower shaft speeds. Evaluation of computed mean film thickness shows excellent agreement with the experimental data. Results show that there is a diminishing reduction of film thickness with an increasing shaft speed. The computational study allows investigation of oil residence time in the annulus near the bearing. Residence time is seen to reduce with increasing shaft speed and with increasing oil flow rate.

This CFD investigation represents the first successful fully coupled two-way ETFM-DPM investigation into the droplet generation process within a bearing chamber application, establishing a firm foundation for future aeroengine bearing chamber modelling.

NOMENCLATURE

Symbol	**Description**
θ	Diameter, m
b	Chamber length, m
Ω	Rotational speed, rpm
T	Temperature, K
$\dot{m}$	Mass flow rate, kg/s
P	Pressure, bar
ρ	Density, kg/m^3
μ	Kinematic viscosity, kg/(m.s)
σ	Surface tension, N/m

Acronyms

ETFM	Eulerian Thin Film Model
DPM	Discrete Phase Model
RPM	Revolutions per Minute
VOF	Volume of Fluid
SST	Shear Stress Transport

Subscripts

sh	Shaft
oc	Outer Chamber
scv	Scavenge
o	Oil
a	Air

1. INTRODUCTION

Within aeroengines, bearings support the shafts and are supplied with oil for lubrication and cooling. Bearing chambers house the bearings, collecting the oil which is dispersed due to the angular velocity of the shaft. Within this highly rotating two-phase environment, it is important that the oil is collected and returned to the tank, avoiding any unnecessary working and overheating of the oil.

Typically, to prevent over-heating, the amount of oil supplied to the bearing, for lubrication, is far greater than needed. Therefore, the capability to accurately model the oil behaviour inside the bearing chamber is key to achieving proper dimensioning of the oil system. Through a low oil residence volume, a more desirable, lightweight and efficient oil system can be achieved.

1.1. Bearing Chamber Investigations

Glahn et al. [2] investigated the oil droplet flow inside an aeroengine bearing chamber for shaft rotational speeds up to 16,000 rpm. Glahn et al. established that the lubricating oil is shed from the roller elements and the cage of the bearing before exiting into the bearing chamber. This turbulent oil-air flow presents a highly complex two-phase environment. The work of Gorse et al. [3] and the more recent high speed camera investigations of both Santhosh et al. [4] and Hee et al. [5] have revealed that, depending on the shaft rotational speed, oil is shed as a combination of droplets, ligaments, sheets or a fine mist. Droplets impinge on the stationary outer walls, leading to the formation of a continuous thin film, which is subsequently driven by both the gravity and shearing air flow forces.

Glahn and Wittig [6] were able to successfully characterise the turbulent nature of the oil film on the stationary outer walls through experimental film velocity measurements over shafts speeds in the range of 3,000-12,000 rpm. Kurz and Baur [7] experimentally investigated the influence of shaft speed on the oil film formation, which revealed two distinct oil flow regimes. The first regime, identified at lower shaft speeds, is a gravity driven oil flow resulting in a very thin oil film on the stationary wall, with only minor air flow interactions. At higher shaft speeds, the second regime is dominated by the shearing air flow, forcing the oil film on the chamber walls to rotate. Within this shearing flow regime, Eastwick et al. [8], demonstrated within the wake of geometric features, dry-out regions can occur. Chandra et al. [9, 10] performed experimental investigations into the sump regions of a bearing chamber, highlighting the importance of a sump geometry on the oil residence volume, identifying key features that affect the efficiency of oil removal from the system.

In order to assist the development of CFD capability for bearing chambers, it is first necessary to highlight the relevant flow phenomena. Within a bearing chamber, the detailed physics may be broken down into two distinct but interacting regions. Firstly, a segregated flow region, characterising laminar wavy oil films with varying film thicknesses, driven by shear and gravitational forces. Secondly, a dispersed flow region, consisting of oil droplets with a range of different sizes that are transported by the turbulent gas flow. As such, the following provides a review of the modelling capability for segregated flows within a bearing chamber; Part II, [11], of our current investigation focuses on modelling of the dispersed flow and the advantages of couplings with a discrete phase modelling (DPM) approach.

Traditionally the Volume of Fluid approach (VOF) has been employed for bearing chamber CFD investigations. The VOF method is able to capture the highly complex three-dimensional recirculating flow structures observed experimentally. More recently for VOF simulations, Bristot et al. [12, 13] highlighted the importance of the turbulence damping parameter on the final overall state of the bearing chamber flow regime observed. For example, moving from a value of 100 towards the default value 10, the smooth flat film regime transitions to a wavy unstable film. A quantitative comparison of film thickness measurements to experimental data revealed that both cases investigated by Bristot et al. showed poor agreement. This suggests that over the wide range of bearing chamber flow regimes observed there is no universally comprehensive value for the turbulence damping factor. Thus, presenting a critical problem for future bearing chamber VOF simulations. To date, the technique implemented by Bristot et al. [13] with a turbulence damping factor of 100 is regarded as the best practice approach.

Prior computational research has demonstrated the capability of film modelling using a VOF approach. However, this best practice methodology does not account for the effects of droplet interactions either through splashing, stripping and to some extent edge separation. The amount of droplets generated and their size distributions are unclear, for which subsequently, it is unknown how their transport and deposition influences the film flow and its development. Whilst for predominately segregated flow regimes a VOF approach is suitable, it is not feasible for cases involving mixed flow regimes, i.e. segregated film flows with a dispersed droplet flow. Furthermore, within a bearing chamber, far from the sump on the stationary outer walls, the formation of a thin oil film can be observed, [3–5]. For a VOF approach, Bristot et al. [13] recommended a minimum mesh resolution of at least 4 grid cells within the oil film; which therefore in order to resolve a thin film would require a very fine interface, becoming extremely costly.

The ETFM, due to its two-dimensional nature, is well suited to resolving thin films, permitting a much coarser grid spacing and hence presenting a significant computational saving compared with the VOF model. Mathematical studies on rimming flows, [14–16], have shown the capability of accurately predicting the smooth, shock and pool solutions through a more rigorous formulation and the inclusion of inertia effects. In addition, a clear link between surface tension and solution stability was highlighted. Subsequent numerical studies on rimming flows, which are analogous to an idealised bearing chamber, have been performed by authors such as Kay et al. [17] and Kakimpa et al. [18, 19]. Kakimpa et al. [19] was successfully able to model the smooth, shock and pool steady flow regimes. Both the amount of liquid present and predominately a balance between the gravitational, viscous and interfacial shear stresses determine the flow regime. When the interfacial shear stresses are enough to overcome the gravitational forces, the smooth flow regime is observed. Conversely, when the gravitational force is greater than this shear force, the pool regime is obtained. The shock flow regime can be observed when transitioning between these two flow states.

Whilst the ETFM is capable of accurately resolving thin films within bearing chambers, in regions of thick films such as near the sump, it is unacceptably inaccurate. Recently Kakimpa et al. [20, 21] developed a methodology to transition between VOF and ETFM with excellent results and cost savings, demonstrating the capability on a representative bearing chamber model. Through a coupled VOF-ETFM model, accurate predictions of the thin film can be achieved on grid resolutions typically much coarser than a standard VOF method, away from which, in the rest of the domain, the VOF approach is retained. Kakimpa et al. performed a qualitative comparison but little information surrounding the performance of the coupled model was acquired. More recently Singh et al. [22] performed a quantitative analysis for the VOF-ETFM model within a simplified bearing chamber geometry, comparing to experimental data. The ETFM-VOF approach was able to qualitatively capture the oil film formation and distribution on the outer chamber wall, however, in general under-prediction of the film thickness was observed. Furthermore, Singh et al. [23] also employed the coupled VOF-ETFM model to a wetting and drying bearing chamber case study. An additional source term was included within an enhanced-ETFM formulation in order to resolve the contact angle effect. The performance of the model was first assessed for a flat plate geometry with excellent results, demonstrating the qualitative trend of capturing rivulets. When applied to a bearing chamber geometry, the ETFM again under-predicted the film thickness but good qualitative trends of film thickness formation and distribution were observed.

The objective of this paper is to investigate the detailed flow physics of the droplet generation process within an aeroengine representative bearing chamber using a two-way ETFM-DPM coupling. Although there are some experimental studies to date surrounding the rotational shaft speed and the influence of air on the oil film, the air-oil interaction itself is not well-understood. A two-way coupling is implemented and investigated such that Lagrangian droplets can be transferred to a thin film through impingement but can also be removed from the surface of the film due to either, splashing, film stripping or edge separation. This work will build upon the existing modelling capability developed by Nicoli et al. [1], in order to improve understanding and investigate new flow physics for aeroengine bearing chamber modelling.

2. BEARING SHEDDING RIG

The geometry presented in this study reproduces the front bearing chamber found in the experimental investigations into an aeroengine representative ball bearing by both Santhosh et al. [4] and Hee et al. [5]. A schematic of the test rig is provided in Figure 1. The bearing oil shedding rig has an annular shape, with a rotating truncated shaft capable of shaft speeds up to 7,000 rpm. Oil is fed to the test bearing at three underrace locations.

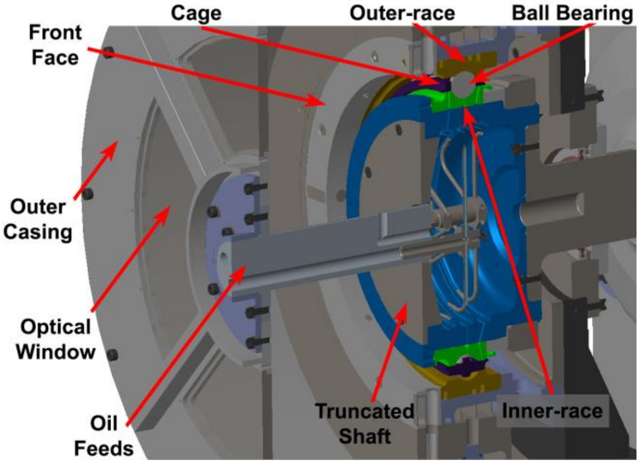

FIGURE 1: SCHEMATIC OF BEARING OIL SHEDDING RIG [5]

Figure 2 shows a cross-section of the front bearing chamber geometry modelled for the aeroengine ball bearing under investigation.

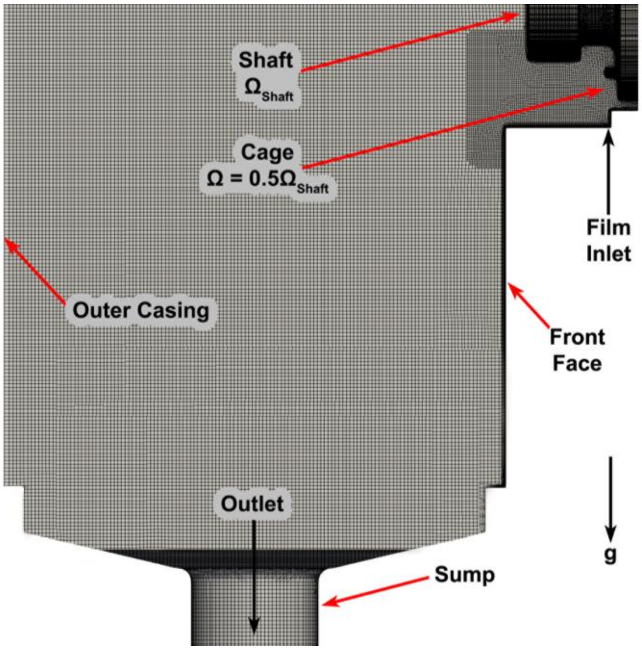

FIGURE 2: CROSS SECTION OF HEX-DOMINANT MESH

A hex-dominant mesh was generated within ANSYS Mesher using a cut-cell approach and care was taken to suitably refine the boundary layer. In order to avoid simulating the test ball-bearing, the computational domain starts at the edge of the cage, closest to the ball bearing. To further reduce the simulation complexity, a representative film inlet boundary condition is proposed, which starts beyond the sharp corner of the outer race as shown in Figure 3. It is therefore assumed that all of the oil exiting past the bearing cage impinges on this stationary outer wall, much like the flow past the edge of a rotating cup as observed experimentally by Santosh et al. [4]. Therefore, all of the oil is fed from this inlet location, the disadvantage being, that the momentum exchange of the oil droplets impinging on the surface from the cage wall is therefore ignored, potentially resulting in a reduced film velocity. As such, an alternative, more comprehensive, film inlet boundary condition is also explored in Section 4, whereby oil is supplied as a thin film at the outer-race location and also a DPM source at the cage-edge. For both cases, at this inlet location, oil is supplied into the domain based on the experimental measurements of Hee et al. [5] and given a rotational velocity derived from the VOF investigations performed by Adeniyi et al. [24] into the same ball bearing representative configuration.

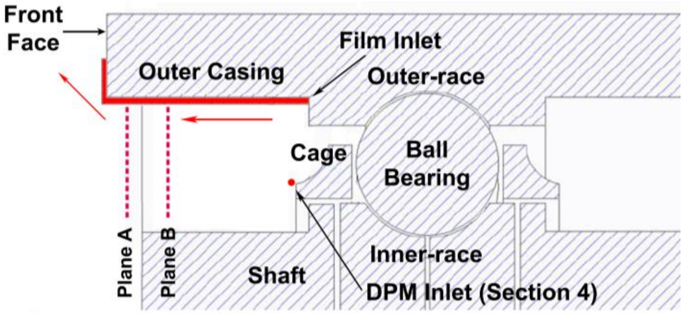

FIGURE 3: CROSS SECTION OF FILM INLET AND AXIAL MEASUREMENT PLANES, MODIFIED FROM [5]

Experimentally, and within Figure 3, the film thickness is measured at planes A and B. Upstream of the front-face edge, these measurement planes are located at an axial distance of 3mm and 10mm respectively; the 0 location corresponds to the front face edge.

Using high speed imaging, Santhosh et al. [4] and Hee et al. [5] investigated two angular positions around the bearing chamber annulus, both 90° and 270° locations which are denoted as P2 and P4, as shown in Figure 4.

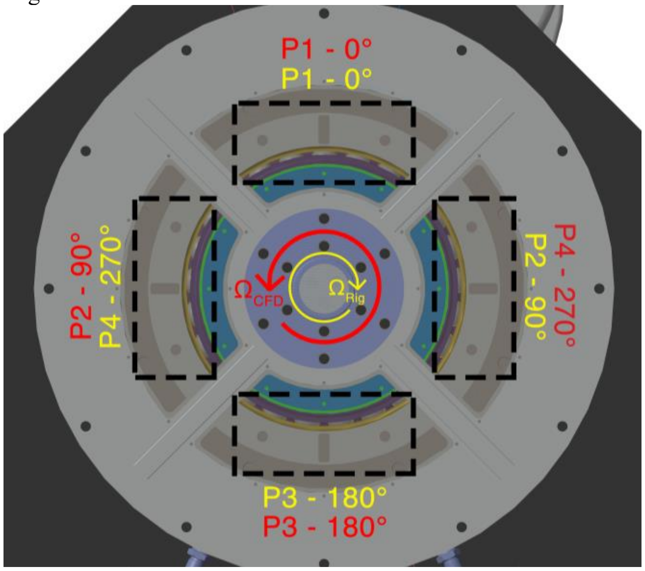

FIGURE 4: CONVENTION FOR ANGULAR POSITIONS

At the P2 location, gravity acts parallel to the air-oil interfacial shear and is therefore regarded as the co-current side. Conversely, at the

P4 location, the counter-current side, gravity acts against the circumferential shear. Furthermore, with reference to Figure 4, location P1 refers to the top of the chamber at 0° and the P3 location corresponds to the bottom of the chamber at 180°. However, computationally, due to a misinterpretation, the shaft rotation is applied in the anti-clockwise direction (red), as shown in Figure 4. This therefore means, that when facing the front of the rig, the P2 region is now located on the left-hand side of the chamber, and conversely, the P4 section on the right-hand side. Overall, this implication has no effect on the results, however, to ensure consistency the P2 computational region is always compared with the P2 experimental region and vice versa; the same is true for the P4 sector.

Initially, a single phase, air-only, mesh independence study was conducted with 4 grids generated using baseline cell sizes of 4mm, 3mm, 2mm and 1mm. Bodies of influence were used to refine the mesh by up to 2 levels in regions where there were high gradients of flow variables, such as the initial gap between the shaft and stationary outer casing, where the film first develops. Equally, the mesh was coarsened in locations far away from the oil phase, such as the static central tube, which experimentally houses the oil delivery system. Inflation layers were applied to sufficiently refine the walls towards the shaft edge and also near the stationary outer casing to appropriately resolve the oil film, achieving a wall spacing of $y^{+}< 1$. Analysis of film thickness measurements, at several different angular and axial locations showed small differences between the two finest meshes at 7,000 rpm. However, at a shaft speed of 12,000 rpm, severe convergence stability issues were faced for the mesh with a core cell sizing of 2mm and a stable solution was not achieved. Consequently, the finest mesh at a core cell sizing of 1mm and a total count of 35 million cells was chosen for all two-phase simulations, in order to maintain consistency across all shaft speeds.

For two-phase flow, an investigation into applying rotational periodicity was unsuccessful, resulting in a wave-like structure imposed on the surface of the thin film depending on the degree of periodicity. In a periodic annulus, with the inclusion of a gravity body force, the gravity component transforms into a rotational force acting to accelerate the film in the direction of the shaft rotation; as such the film exiting one periodic boundary is not a true representation of the film entering the opposing periodic boundary. Furthermore, it is also not possible to represent the sump outlet boundary condition in a periodic mesh. Without the sump, the thin film builds up on the stationary outer casing walls leading to pooling and a thick film, for which the ETFM is insufficiently accurate. At higher rotational speeds where the shear driven air flow dominates the force due to gravity, it may be possible to use rotational periodicity, however for the present study the full 360° domain is modelled.

2.1. Computational Setup

The operating conditions were chosen to represent the experimental conditions employed by Hee et al. [5]. Three different rotational shaft speeds were investigated, for which at each speed, two different oil flow rates were studied. Experimentally, the lubrication oil chosen was Aeroshell Turbine Oil 390, fed at a fixed temperature of 35 °C, which heated up to an average temperature of 60 °C as it passed through the bearing. Table 1 summarises the operating conditions and material properties employed computationally.

Experimentally, Santhosh et al. [4] and Hee et al. [5], investigated rotational shaft speeds up to 7,000 rpm. However, for the present computational study, in order to investigate more realistic engine speeds, this range has been extended to 12,000 rpm for both oil flow rates. Image analysis conducted by Santhosh et al. [4], determined the cage speed to be approximately 50% of the shaft rotational speed. Within the experiment, the induced local air flow is only due to this rotational speed from both the shaft and bearing cage. As such, computationally, both the shaft and cage shown in Figure 3, are represented as rotating walls whilst the other walls remain stationary.

TABLE 1: COMPUTATIONAL OPERATING CONDITIONS AND MATERIAL PROPERTIES

Shaft rotational speeds	Ω	5,000 7,000 12,000	rpm
Air temperature	T_a	333.15	K
Oil inlet temperature	T_o	333.15	K
Oil inlet volume flow rates	$\dot{m}_o$	5.2 7.3	l/min
Chamber absolute pressure	P	1.01	bar
Material Properties			
Air density	ρ_a	1.059	kg/m^3
Air viscosity	μ_a	2.008×10^{-5}	kg/(m.s)
Oil density	ρ_o	890.8	kg/m^3
Oil viscosity	μ_o	0.00681	kg/(m.s)
Oil-air surface tension	σ	0.0302	N/m

Not all of the oil supplied to the bearing exits into the front chamber. On the test rig, oil is supplied to three underrace locations, at the front, middle and rear of the bearing. The flow rate through each of these locations is independently controlled, such that the proportion of oil supplied is 1:1.33:0.67 respectively, chosen as an engine-representative split. Over each rotational speed, testing was conducted over two flow rates: namely 5.2 l/min and 7.3 l/min. Over all of the rotational speeds investigated experimentally, approximately 89% of the oil exits through the front chamber sump [5], meaning that computationally, the flow rates of oil supplied to the front chamber are 4.6 l/min and 6.5 l/min respectively.

As shown in Figure 3, the film inlet starts beyond the sharp corner of the outer race. Within OpenFOAM, at the film inlet, quantities for both the film thickness and film velocity were specified. Film thickness quantities are determined through linear interpolation of the experimental film thickness measurements of Hee et al. [5], for each combination of rotational speeds and flow rates investigated. For the 12,000 rpm cases this is predicted from the experimental data based on the observations of Hee et al. [5]. Film inlet velocities are derived using the work of Adeniyi et al. [24] who presented a VOF computational study of the oil-air flow within the same aeroengine ball bearing. The authors provide oil speed measurements towards the front bearing chamber over a combination of two shaft speeds and two oil flow rates: 5000 and 13,000 rpm for 4 and 8 l/min respectively. Adeniyi et al. report that, over all of the cases investigated, the oil slows down, exiting past the bearing cage into the chamber at roughly 10% of the shaft speed. Knowing the film thickness around the chamber annulus, the oil mass flow rate and hence volume flow rate, these can be used to determine the axial velocity of oil into the domain. Finally, the tangential velocity component is calculated to make up the remaining 10% of the shaft speed.

In previous bearing chamber experimental investigations, Gorse et al. [3], demonstrated that a differential pressure drop across a roller bearing had a significant impact on the way oil was shed from the bearing. As such, in order to eliminate this factor, during the experiments of Santhosh et al. [4] and Hee et al. [5] the pressure difference across the bearing was minimised and the rig operating pressure was maintained close to ambient. Oil shed from the bearing is gravity scavenged, such that the scavenge pipe can therefore be represented as a pressure outlet at ambient conditions, also acting as a film outlet for the ETFM.

2.2. Numerical Settings

For the three shaft speeds under consideration, initially a single-phase steady-state solution was first obtained using simpleFoam, after which a transient single-phase solution was achieved using pimpleFoam. This transient single-phase solution was used as the initial condition for all of the following two-phase simulations within the *sprayParcelFilmFoam* solver.

sprayParcelFilmFoam [1] is an in-house, fully coupled two-way ETFM-DPM compressible, transient solver with models for both primary and secondary atomization of the particulate cloud. The solver incorporates two newly developed and validated thin film sub models for both a film stripping and an edge separation criteria. In our previous work, *sprayParcelFilmFoam* [1] was developed for modelling of oil jet-breakup and the subsequent film formation intended for bearing chamber applications. *sprayParcelFilmFoam* and the relevant sub-models were validated against an experimental case study, significantly improving on the previous state-of-the-art modelling capabilities. The work carried out in this paper is the first application of *sprayParcelFilmFoam* to an aeroengine representative bearing chamber.

The PIMPLE algorithm is used to solve the pressure-velocity coupling, with *nCorrectors* and *nOuterCorrectors* set to 3 and 50 respectively, such that convergence of the pressure, velocity and turbulent quantities are instead controlled using a residual convergence criteria of 1×10^{-6} for the maximum average. Overall, simulation convergence criteria is primarily assessed through monitoring the oil residence volume on the stationary outer casing wall. A steady state solution of the oil can be assumed once the oil residence volume fluctuates periodically around a constant average value. Typically, a steady solution was achieved after a flow time of 1.0 s, after which data was temporally averaged over a further 1.5 s; approximately 5 film cycles from inlet to edge. A second order upwind-biased discretization scheme was chosen for all pressure, momentum, turbulence and surface film terms. The time discretization scheme uses the Euler transient, first order implicit, bounded scheme.

For industrially relevant flows, such as bearing chamber applications, the current state-of-the-art turbulence modelling approach is to use the SST k-ω turbulence model as demonstrated by both Bristot et al. [12] and Singh et al. [22]. As such, for the purpose of this work, the SST k-ω turbulence model was used for all simulations.

The solver was implemented with parallel capabilities, using the scotch decomposition method, most calculations used 40 to 200 CPU cores.

2.3. ETFM-DPM Coupling

The following section provides a brief overview of the ETFM-DPM governing equations present within *sprayParcelFilmFoam*; a complete review is presented by Nicoli [25].

Within OpenFOAM, the thin film model was first implemented by Meredith et al. [26]. Due to the thin nature of the film, 2D continuity and momentum equations can be solved to obtain the film thickness and wall-tangential velocity components. Integrating over the film height, the momentum transport equation becomes:

$$\frac{\partial \rho_l \delta \boldsymbol{u}_f}{\partial t} + \nabla_s\left[\rho_l \delta \boldsymbol{u}_f \boldsymbol{u}_f\right] = -\delta \nabla_s p + \boldsymbol{S}_{\rho_l \delta \boldsymbol{u}_f} \tag{1}$$

Here, the momentum source terms are comprised of both pressure-based and stress-based forces. The capillary effects, p_σ, due to surface tension, hydrostatic pressure head, p_δ, due to gravity and the local gas-phase pressure, p_g, comprise of the forces within the pressure term, p. Whereas, the gravity body force, $\rho g_\theta \delta$, the contact-angle force, τ_θ, and the viscous shear stresses at both the film-gas interface, τ_g, and the film-wall interface, τ_w, make up the stress term, $\boldsymbol{S}_{\rho_l \delta \boldsymbol{V}_f}$.

Whilst Eulerian continuum equations are solved using a conservation of momentum approach for the fluid phase, discrete phase modelling employs a Lagrangian particle tracking approach. Whereby particle trajectories are determined through evaluating Newton's equations for the particulate phase. For the present work a two-way turbulence coupling is enabled to account for the force exerted by the particles on the fluid and vice-versa. As such the following equation is solved to obtain the particle trajectories:

$$m_p \frac{d\boldsymbol{u}_p}{dt} = \boldsymbol{F}_p \tag{2}$$

Here, m_p and $\boldsymbol{u}_p$ represent the particle mass and velocity respectively. $\boldsymbol{F}_p$ represents the sum of forces acting on the particle. For a standard spherical particle:

$$\boldsymbol{F}_p = \boldsymbol{F}_D + \boldsymbol{F}_g + \vec{\boldsymbol{F}} \tag{3}$$

Where $\boldsymbol{F}_D$ represents the drag force, this is the dominant force that determines the particle trajectory. $\boldsymbol{F}_g$ is the gravity and buoyancy force and $\vec{\boldsymbol{F}}$ represents any external forces acting on the particle, which for this case study are none. Once the particle force, $\boldsymbol{F}_p$, has been calculated, through integrating the particle velocity, the trajectories are determined.

Within the bearing shedding rig, the fully coupled ETFM-DPM approach can be broken down as follows. Oil is supplied into the domain using an ETFM inlet, Figure 3, as such, a thin film develops over the outer casing wall. Due to the high shearing gas velocities, droplets can be stripped from the surface of the film, requiring the use of a film stripping model. Once the film reaches the front face-edge, the momentum of the oil causes a proportion of the liquid to separate as droplets, whilst the rest of the film remains attached and flows down the front-face; to account for this behaviour, an edge separation model is included. Droplets travelling through the air may experience secondary breakup as a result of the high shearing gas forces. Subsequently, these droplets will impinge on the outer casing wall forming a thin film and potentially splashing. Finally, the film is removed from the system through the gravity scavenge arrangement.

Part II, [11], of our current investigation focuses on the droplet behaviour near the bearing and as such a more detailed analysis of the oil droplet modelling is presented, including the criterion for secondary breakup, stripping and edge separation.

3. RESULTS

3.1. Qualitative Oil Distribution

Figure 5 shows mean velocity vectors of the oil film within the slot after the bearing, as such, the mechanism for oil formation on the stationary outer cylinder wall, highlighted in Figure 3, can be observed. Within Figure 5, observation of the co-current side shows that the direction of the oil film is significantly more uniform compared to the counter-current side. This can be accounted for, since within the P4 region, the interfacial rotational shear acts in the opposing direction to the downward force due to gravity. As a result, there is a reduction in the tangential velocity component in the counter-current oil film, causing a flow reversal as the film is pulled back downward. The incoming upstream oil mass, which is flowing axially outward, therefore causes the oil film to intermittently undulate resulting in a non-uniform wavy film compared with the P2 co-current side.

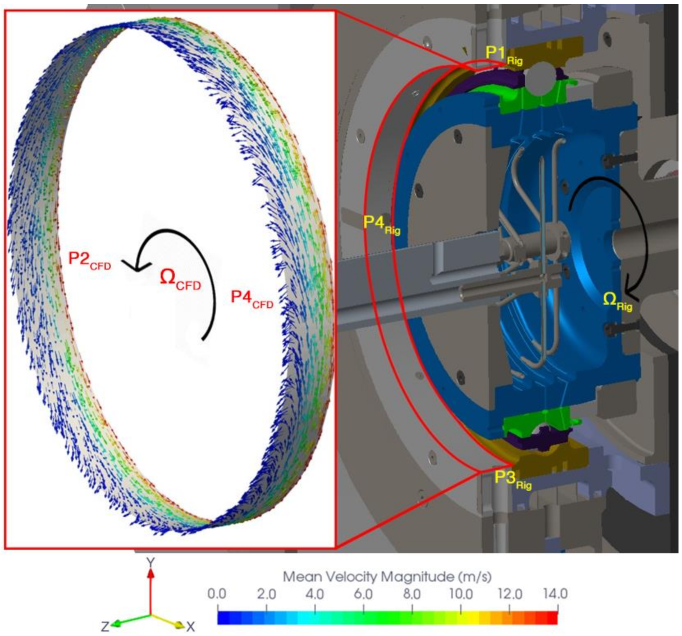

FIGURE 5: FILM MEAN VELOCITY VECTOR PLOT AT 7,000 RPM AND 7.3 L/MIN

Figure 6 shows a view of the front face, highlighted in Figure 3, and an instantaneous film thickness measurement due to the attached film as it flows over the corner, in part due to this undulation effect.

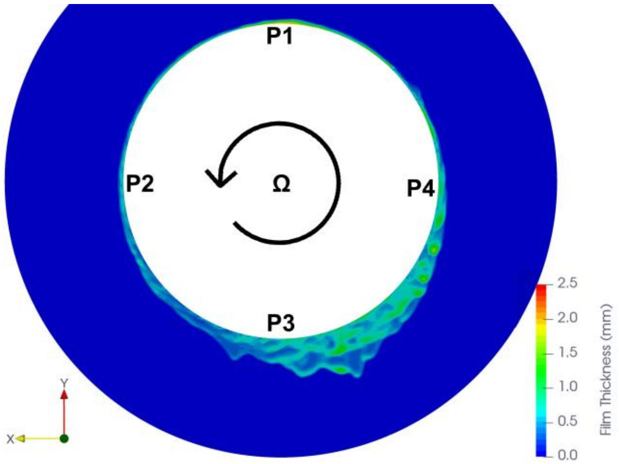

FIGURE 6: INSTANTANEOUS FILM THICKNESS ATTACHED ON THE FRONT FACE AT 7,000 RPM AND 7.3L/MIN

Over a sharp edge, liquid may separate from the surface, whilst a proportion may turn the corner and still remain attached. The amount of mass to be separated is dependent on the critical force ratio, derived from a force balance between the film inertia, surface tension and body forces. From Figure 6, it is apparent that at P2, the co-current region, very little mass remains attached, suggesting that that the critical force ratio is satisfied and the liquid becomes separated as droplets. Conversely as we move around the chamber from the P3 to the P4 sector, a larger proportion of mass remains attached and flows over the edge. Upstream of the edge, the film velocity slows as it is pulled downwards due to the effect of gravity and therefore does not have sufficient inertia to fully separate from the edge. Instead, waves of film fall over the edge due to the undulating effect of the upstream flow reversal, shown in Figure 5.

Computationally, these effects of undulation and film slowing can be observed in Figures 7a-c. For all of the shaft speeds investigated, Figures 7a-c show the mean film velocity magnitude vector plots for the P4 counter-current side; the P2 co-current region is not shown, since for all cases a smooth shear flow was observed, much like in Figure 5. For clarity only the last section of the film is shown and a reference location for Plane B is highlighted for comparison to the experimental measurement plane which is located at an axial distance of 10mm from the front-face edge.

Within Figures 7a-c, only the higher oil flow rate at 7.3 litres per minute is shown for simplicity, although comparable results were observed for the cases at a flow rate of 5.2 litres per minute. For the counter-current region it is observed that the oil velocity changes direction as it is pulled downward due to the gravitational force. When the gravity component is equal to the shear effect, the flow field transitions to a shock regime and the observed undulation effect reaches a maximum. Within bearing chambers, a shock regime refers to the transitional period when the gravity dominated pool flow moves toward a smooth shear dominated flow. Beyond this critical point, when the shear force dominates the gravitational force, a further flow reversal within the counter-current region is observed and the waves begin to travel upwards with the direction of the shaft rotation.

The experimental investigations of Hee et al. [5] revealed that, at the observational measurement plane B, the critical speed at which this second flow reversal takes place is observed between 3,000 and 5,000 rpm, beyond which the shear-dominated smooth flow regime is witnessed. From the experiments of Hee et al., it is not reported whether this observation is also apparent at Plane A, 3mm upstream of the front face-edge. However, computationally, from Figures 7a-c, at the Plane B location, the film is travelling upwards suggesting a smooth shear dominated flow regime, much like the experimental observations of Hee et al. [5]. Immediately afterward we can see the effect of gravity pulling the film downward suggesting that this shear dominated smooth flow regime has not been fully reached at the counter-current side. Even at 12,000 rpm, Figure 7c, a transitional period within the shock regime is observed, with oil waves towards the top of the chamber traveling upwards, and waves seen to be pulled slightly downward at the bottom of the chamber. Since the bearing chamber runs with a truncated shaft, as depicted in Figure 1, it may be possible that this smooth shear dominated flow regime is not achievable, even at 12,000 rpm. As the air flow moves towards the bearing chamber expansion, the shearing velocity decreases and hence the shearing force is reduced, potentially to the point where gravity still dominates. In addition, this effect of the truncated shaft is compounded by the absence of a sealing air flow within the bearing shedding rig, which as previously demonstrated by Gorse et al. [27] for single phase air flow can have a significant effect on the air flow structure.

The reason why, computationally, a fully shear driven smooth flow regime is never reached, may also be attributed to the formulation of the thin film representative inlet boundary condition. Experimentally, the mechanism for oil film formation on the outer stationary cylinder walls can be broken down into two components: oil shed from the cage-edge and the axial displacement of oil at the outer-race location. Without directly modelling the oil breakup from the cage-edge, a significant proportion of the tangential momentum imparted on the oil film could be lost, due to not capturing the momentum exchange of the droplets or ligaments impinging on the surface film. Therefore, this gain in tangential momentum could, in turn, transition the film into a fully shear driven flow regime within the counter-current region. As such, a more comprehensive film inlet boundary condition is proposed and explored later in Section 4.

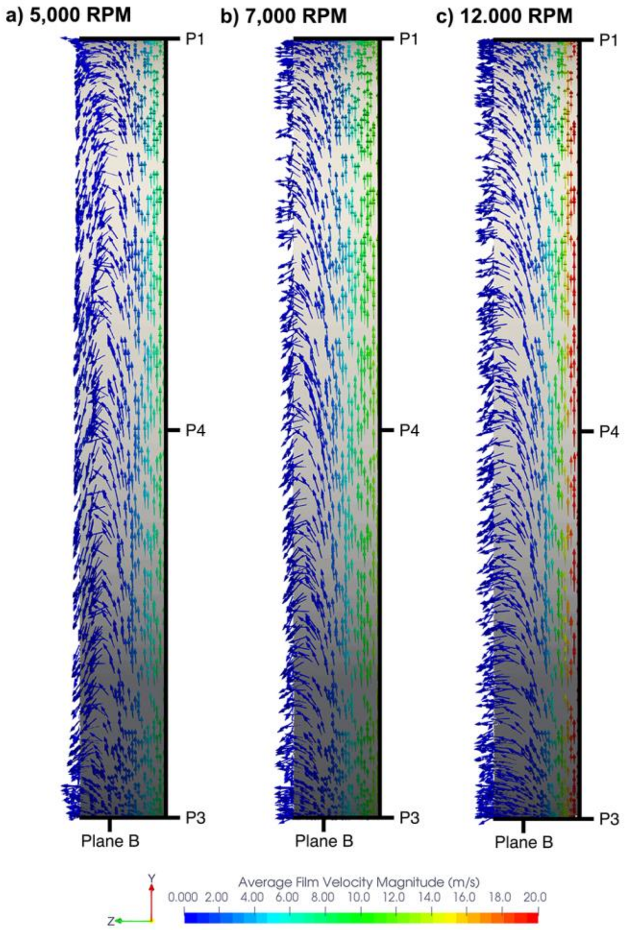

FIGURE 7: MEAN VELOCITY MAGNITUDE VECTOR PLOTS AT EACH DIFFERENT SHAFT RATIONAL SPEED AND 7.3 L/MIN FOR THE P4 COUNTER-CURRENT REGION

3.2. Quantitative Oil Distribution

The axial variation in the average film thickness at the P2 and P4 locations are shown in Figures 8a-f. For all of Figures 8a-f, the axial extent of the film is presented, whereby 0 corresponds to the front-face edge and, for clarity, only the distance over the last 20mm of the film is shown. Experimental film thickness measurements are presented by Hee et al. [5] for both P2 and P4 regions at Planes A and B from the front face-edge, these correspond to the axial location of 3mm and 10mm upstream of the front-face edge respectively.

With an increase in flow rate from 5.2 l/min to 7.3 l/min, comparing Figures 8d-f with Figures 8a-c, at each shaft speed the same overall trend is captured with minor deviations. The most notable difference occurs at 7,000 rpm where at the lower volume flow rate, Figure 8e, a thicker film initially builds up, with both P2 and P4 regions then thinning equally; whereas at 7.3 l/min, Figure 8b, a relatively stable film is formed which again thins. In general, whilst there may be some variations between either the P2 or P4 regions, at the two volume flow rates, the differences are not consistent.

The main trend observed from the film thickness measurements plots is the decreasing film thickness with an increase in rotational shaft speed, again in agreement with the experimental measurements of Hee et al. [5]. This result is expected due to the dependence of the film thickness on the rotational shaft speed; since an increase in speed will increase the circumferential air velocity and hence increase the interfacial shear force. Subsequently the film velocity increases and as a result, the oil film thickness is reduced to satisfy mass continuity. It is important to note that the film thickness is also a local function of both the angular coordinate and axial location on the stationary outer wall. Within the co-current region, for both Planes A and B, Hee et al. report a decrease in film thickness of approximately 50% between shaft speeds of 3,000 and 5,000 rpm; with a further reduction of 25% seen as the speed is increased to 7,000 rpm. Conversely at the counter-current side, the film thickness drops by 60% with an increase in shaft speed from 3,000 rpm to 5,000 rpm; and a further increase in shaft speed to 7,000 rpm subsequently sees a drop in film thickness of approximately 30%.

For all of the shaft speeds and flow conditions presented in in Figures 8a-f, the average film thickness of the oil film ranges between a minimum of 0.4mm up to a maximum of 1.4mm. This is in excellent agreement with the results of Hee et al. who report that above a shaft speed of 5,000 rpm, for all cases investigated here, the film thickness varied between a value of 0.5mm to 1.4mm.

Over the experimental data range investigated, Hee et al. report that for both P2 and P4 regions, the fraction that the film thickness reduces by each time is halved, for every step in shaft speed of 2000 rpm. For example, for the P2 side the film thickness reduces first by 50% going from 3,000 rpm to 5,000 rpm and then reduces by 25% going to 7,000 rpm. Therefore, it is not unreasonable to assume that this trend carries forward, reducing by a further 12.5% up to 9,000 rpm and, for arguments sake, reducing by a final 6.25% moving to 12,000 rpm. Similarly, for the P4 side, this would lead to the series of reductions: 60%, 30%, 15% and finally 7.5%. Figures 9a-d show the experimental variation in film thickness measurements with rotational shaft speed presented by Hee et al. [5]; data is shown for planes A and B. For the purpose of the work carried out here, the results of Hee et al. are extrapolated (dot-dashed lines), to shaft speeds of 9,000 rpm and 12,000 rpm for both P2 and P4 regions following the previous diminishing returns theory. The available computational data is shown in black for the P2 and P4 regions, which are represented by the circles and stars respectively. It should be noted that for both the computational and experimental results, whilst the plot markers represent the discrete shaft speeds investigated, these are connected by lines to show the overall trend.

It is clear that across the data, there is an overall reduction in film thickness when we increase the rotational shaft speed from 5,000 rpm to 7,000 rpm, in line with the experimental measurements of Hee et al. [5]. As an overview and in terms of oil residence volume, moving from 7,000 rpm to 12,000 rpm, we do see an overall reduction in the film thickness within both P2 and P4 regions. Although, this is less clear when looking at the individual measurement planes, which all shows a reduction in film thickness at Plane B, 10mm from the front face-edge, but neither a clear increase nor decrease in film thickness at the Plane A location. This in part can be associated with the inability for both cases at 7,000 rpm and 12,000 rpm never reaching the shear dominated smooth flow regime. From Figures 8e-f, it is apparent that the flow reversal, due to fluid being pulled downward due to gravity, takes place just before the oil film meets the front face-edge before being shed into the bearing chamber. This undulation effect evidently goes through a maximum, i.e. the shock regime, somewhere between both the two shaft speeds and flow rates investigated, hence why the variations are not consistent.

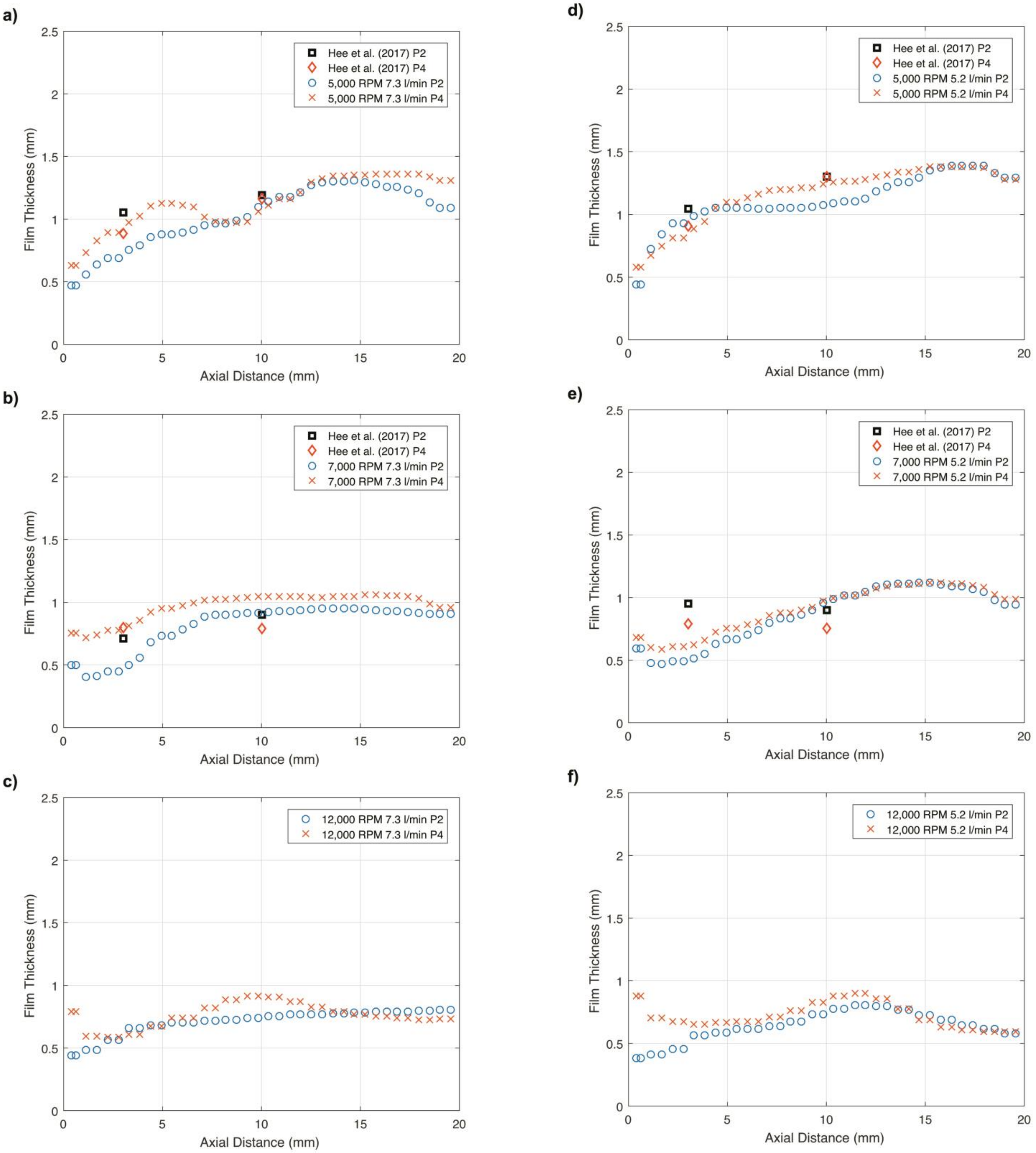

FIGURE 8: AXIAL VARIATION OF FILM THICKNESS AT CO- AND COUNTER-CURRENT REGIONS (P2 AND P4) WITH SHAFT ROTATIONAL SPEED AGAINST EXPERIMENTAL MEASUREMENTS OF HEE ET AL. [5] AT 3MM AND 10MM

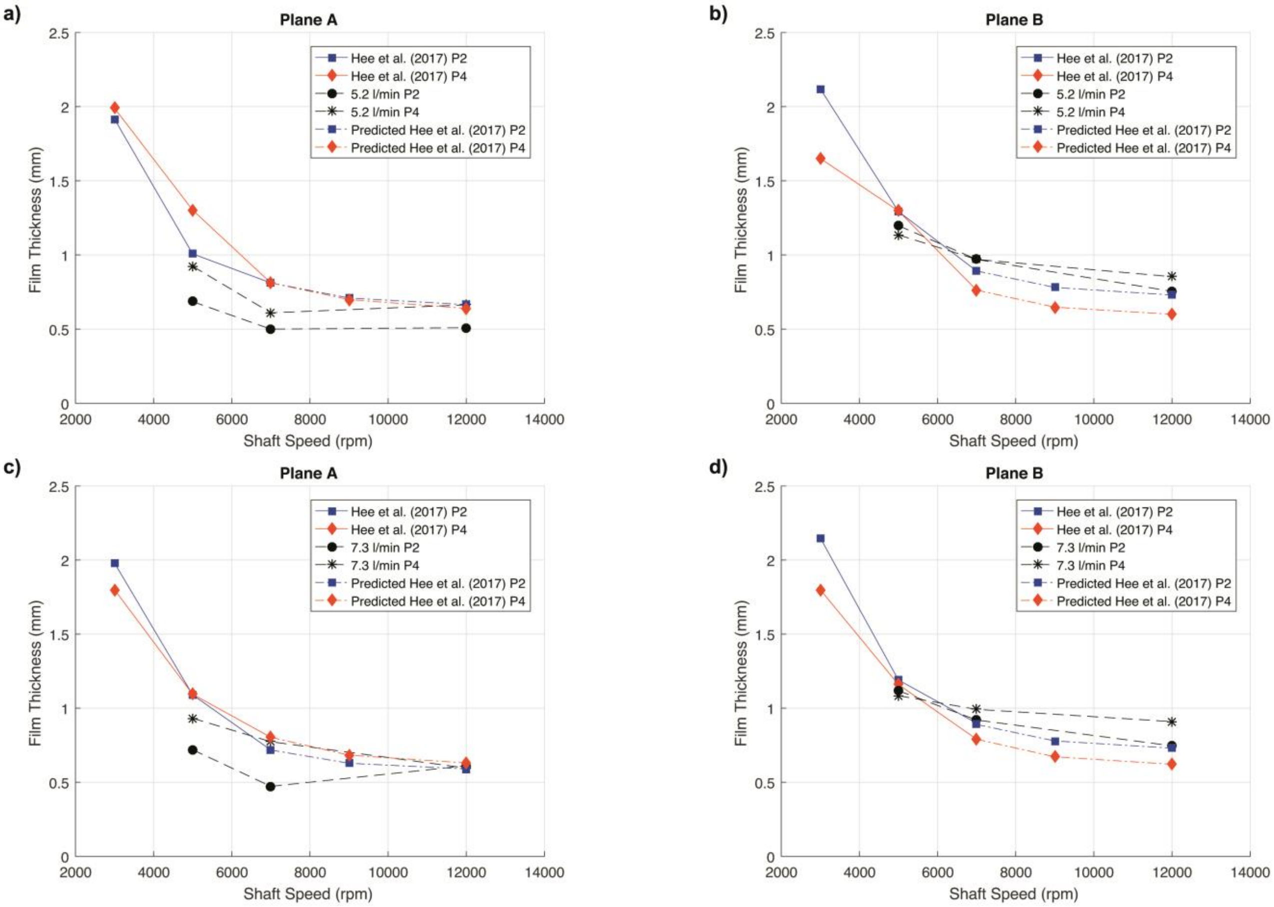

FIGURE 9: VARIATION IN OIL FILM THICKNESS WITH ROTATIONAL SHAFT SPEED FOR CO- AND COUNTER-CURRENT REGIONS (P2 AND P4) WITH EXPERIMENTAL AND PREDICTED MEASUREMENTS OF HEE ET AL. [5]. TOP 5.2 L/MIN AND BOTTOM 7.3 L/MIN.

From Figures 9a-d, for the experimental data points available, the simulations accurately capture the overall trend of decreasing film thickness from 5,000 rpm to 7,000 rpm especially for plane B. Even though at plane A the simulations under predict the film thickness, a good agreement is observed especially without knowing the experimental measurement errors. When the measurements of Hee et al. are extrapolated to 9,000 rpm and ultimately 12,000 rpm, it is clear that the simulations all predict a very similar film thickness. The excellent agreement between the predicted and computational results suggests that there is indeed a diminishing reduction in film thickness with an increase in shaft speed.

3.3. Oil Residence Time

Figures 10a-c show plots of streamlines generated from the mean film velocity, released at both P2 and P4 discrete locations, coloured in red and green respectively. Figure 10a shows streamlines for the shaft speed at 5,000 rpm, for both sides, the film travels approximately the length of one full revolution around the cylinder annulus before exiting into the main chamber; the difference being, that the fluid from the P4 side travels around the annulus eventually undergoing flow reversal within the P4, gravity dominant side. Increasing the shaft speed to 7,000 rpm, as in Figure 10b, as the film velocity increases the distance travelled around the annulus also increases; such that the film now makes over one and a half full revolutions. Finally, at 12,000 rpm, the film travels up two times around the annulus, although all of the distance covered in the initial revolution occurs over the first third of the film where the velocity is at its highest. This becomes apparent from Figure 11, which shows the axial variation of the mean film velocity, non-dimensionalised by the linear shaft speed, over each shaft speed. It is clear that for all cases a significant reduction of film velocity is observed over the first third, reducing from 15% of the shaft speed down to approximately 2.5%, beyond which the film steadily decreases in velocity down to a less than 0.5% of the shaft speed.

It is possible to compare the average oil residence times for each of the three shaft speeds, i.e. the amount of time the oil takes to travel around the annulus before exiting into the chamber. At 7.3 l/min and 5,000 rpm it takes approximately 0.345s for the oil to exit, by 7,000 rpm this reduces to 0.285s and finally 0.275s at 12,000 rpm. Very similar results are observed for the flow rate at 5.2 l/min, with times of 0.335s, 0.27s and 0.26s respectively.

It is expected that for the 5.2 l/min case, the oil residence time will be smaller, since at a fixed shaft speed, with less oil, a thinner and hence faster film will form. However, between the two flow rates a very small difference in oil residence times is observed. This is apparent, since for a given shaft speed, the oil film trends toward the same film thickness at both flow rates, as observed from Figures 8a-f, with the main difference being within the first third of the film development where the velocity is at its highest. Therefore, it is unsurprising that only a small difference in oil residence time is observed between the two flow rates.

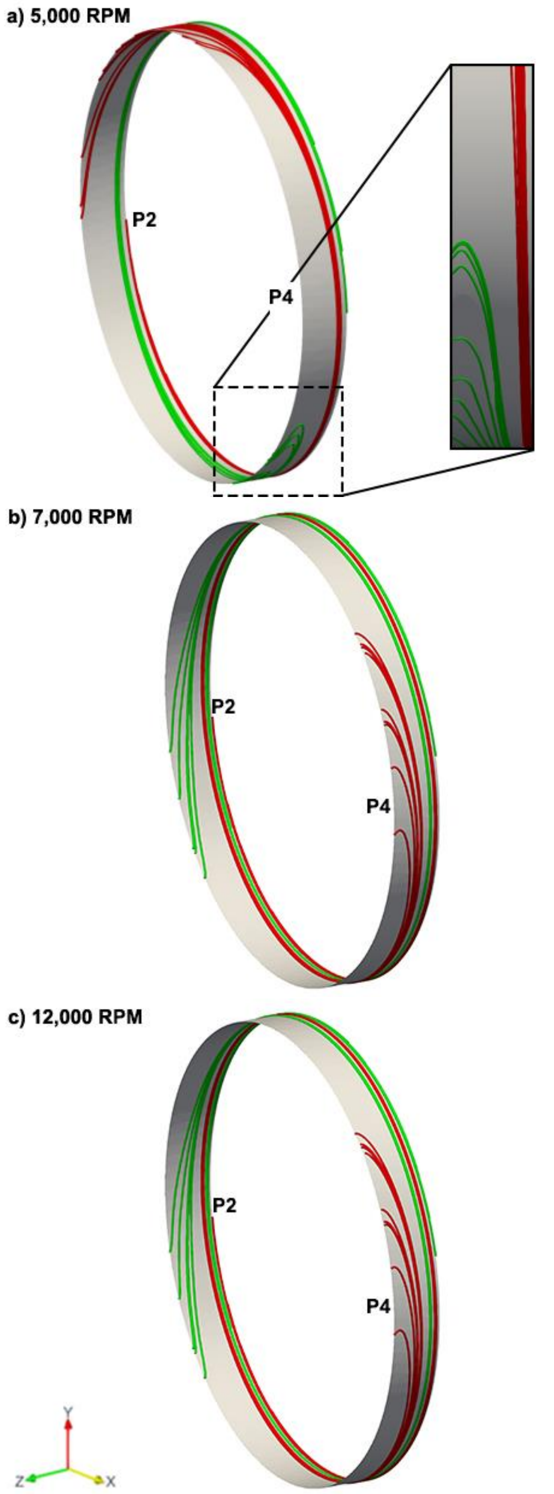

FIGURE 10: MEAN STREAMLINE PLOTS GENERATED FOR P2 (RED) AND P4 (GREEN) LOCATIONS AT EACH SHAFT SPEED (7.3 L/MIN)

Once again it is clear that there is a diminishing return on the oil residence time as the shaft speed increases. It is unclear whether a more appropriate film inlet boundary condition, which would account for the momentum exchange of droplets from the cage-edge, would result in a faster oil film and hence a shorter oil residence time. However, the results show that before the oil separates as droplets into the chamber, there is a maximum residence time of approximately 0.35s, occurring at the slowest shaft speed. This suggests that for bearing chamber design, there needs to be accountability for a minimum oil residence time of at least 0.35s when considering heat transfer effects to prevent oil degradation or coking. In a similar manner, from Figures 9a-d, it is apparent that over both flow rates, due to this diminishing return effect, there is also a minimum average film thickness of roughly 0.4mm, which becomes independent of the shaft rotational speed. Signifying that even beyond shaft speeds of 12,000 rpm and for this flow regime, a dry-out region will not be observed. This also indicates that for future bearing chamber design it is not necessary to distribute oil from the cage-edge in order to prevent a dry-out region.

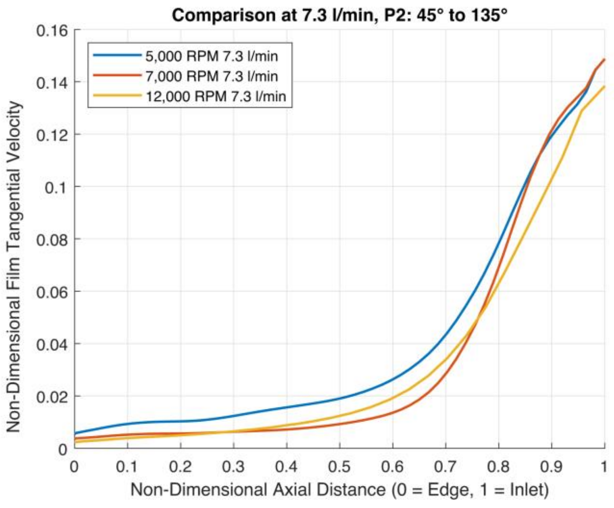

FIGURE 11: NON-DIMENSIONALISED FILM VELOCITY AT THE P2 REGION FOR EACH SHAFT SPEED AT 7.3L/MIN

4. COMPREHENSIVE FILM INLET CONDITION

A concern of the previous work is the modelling assumptions of the film inlet condition. As discussed previously, there are two mechanisms for oil formation on the static outer casing wall, namely: oil shed from the cage-edge and the axial displacement of oil from the bearing at the outer-race. However, there is very limited experimental knowledge surrounding the droplets flung from the cage-edge, either regarding the amount of oil shed, the droplet size distribution or the droplet trajectories. Whilst the oil flow may be analogous to the flow over a rotating cup, due to the relatively smaller size of the cage, there is still considerable uncertainty. As such, originally, a representative film inlet boundary condition was proposed, as outlined below, however as explained it is unclear whether a more comprehensive boundary condition is required.

Representative Film Inlet Boundary Condition: for the initial modelling, it was assumed that all of the oil exiting from the cage-edge impinges on the film surface. As such, all of the oil was supplied axially into the domain at the outer-race location, as depicted in Figure 3. However, the momentum exchange of droplets impinging on the film surface, shed from the cage-edge, are effectively ignored. It is suspected that this may have a significant impact on the overall film velocity, which could potentially lead to a thinner film but also be a factor in achieving a fully shear driven flow regime. As such, a more comprehensive film inlet boundary condition is investigated to assess the effects of including droplets shed from the cage-edge.

Comprehensive Film Inlet Boundary Condition: here, the oil exiting from the bearing is modelled by including both the oil displaced axially from the bearing at the outer-race and also droplets shed from the bearing cage-edge. Firstly, the film developing as a result of oil exiting at the outer-race is generated in the same way as the representative film inlet boundary condition. However, to simulate droplets produced around the periphery of the cage-edge, a DPM injection condition is implemented, to capture the momentum exchange of droplets with the oil film. As such, the volume flow rate of oil needs to be split accordingly between the two oil inlets.

However, there is no experimental data reporting the proportion of oil shed from the cage-edge compared to that axially displaced at the outer-race location. From visual analysis of the experimental results of Santhosh et al. and Hee et al. [4, 5], the cage-edge produces a much smaller fraction of the total amount of oil. As such, three different oil flow rate splits are investigated, a 10/90 percent split of oil from the cage-edge vs outer-race axial displacement and both a respective 20/80 and 50/50 percent split.

Initially, for this comprehensive film inlet boundary condition, the case setup only considered a shaft speed of 7,000 rpm and an oil flow rate of 7.3 l/min. At the cage-edge, oil is supplied via a DPM injection around the full annulus of the cage-edge. In this, the droplets are given a mass flow rate based on the derived percentage split. Analogous to flow past the edge of a rotating cup [4], it is assumed that droplets are dispersed tangentially outward with a velocity equivalent to the cage speed, with no radial or axial velocity component. Since no information is available regarding the size and distribution of the droplets, it is assumed to be equivalent to the droplet distribution stripped from the film surface. This is derived based on the initial simulations using the representative boundary condition. As such, a droplet size distribution is provided based on a log-normal Rosin-Rammler distribution; specifying an average diameter of 55μm and a maximum droplet diameter of 100μm. Using this information, the DPM injection is fully prescribed; and, to account for the reduced volume flow rate of oil at the outer-race, the film inlet velocity is adjusted accordingly.

4.1. Results

To begin with, results were unobtainable for the simulation run with a 50/50 percent split, due to severe numerical instabilities faced as a result of the large proportion of mass injected into the system. However, results were obtained for the 10/90 and 20/80 percent splits and the axial variation in the mean film thickness at the P2 and P4 locations are shown in Figure 12. Only the axial extent over the last 20mm of the film is shown, whereby 0 corresponds to the front-face edge. Immediately it is clear that over both oil splits, poor agreement is found between the experimental measurements of Hee et al. [5], and no significant improvement is found over the previous film inlet boundary condition, as presented earlier in Figure 8b. However, it should be noted that good agreement is observed for the 10/90 percent split within the P2, co-current region. Furthermore, within the P4, counter-current side good agreement is observed up towards Plane B, but beyond which, there is a significant spike in film thickness. As the split is increased to 20/80 percent, the errors that were noticeable in the 10/90 split are multiplied even further and therefore it is unsurprising that at a 50/50 percent split numerical instabilities were faced.

Through injecting oil at the cage-edge, with a speed equivalent to the cage, i.e. half the shaft speed, the particles are carried by the turbulent air flow and impact immediately after the injection location. These particles rapidly accelerate the oil film which leads to a sudden thinning and a trough of oil, resulting in a minimum film thickness of 0.4mm. Downstream of this location, at the 20mm location the film begins to recover and overall there is no comparable difference between the film velocity profiles observed for the two film inlet conditions. In general, the main difference being that this initial acceleration of film causes a much more unstable film to develop downstream, with short waves of oil travelling around the annulus. Comparison of the mean oil mass over the outer cylinder annulus also showed negligible differences between the two film inlet boundary conditions.

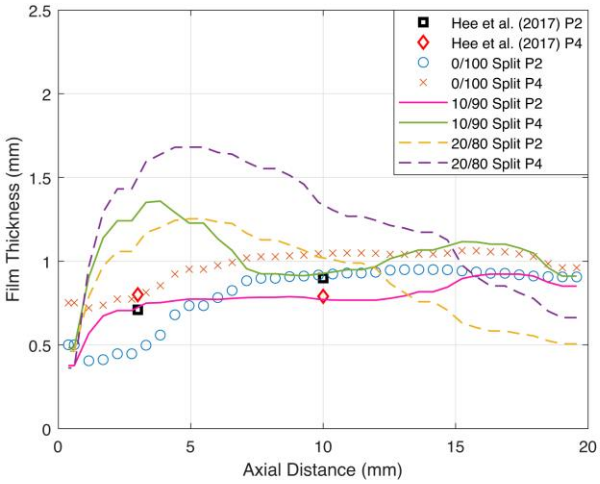

FIGURE 12: AXIAL VARIATION OF FILM THICKNESS FOR TWO OIL INLET SPLITS AT BOTH P2 AND P4 REGIONS

For the more comprehensive film inlet condition, over both oil splits investigated, within the P4 region, a shear dominated flow regime is observable at Plane B, similar to the experimental investigations of Hee et al. [5]. However, beyond this, the presence of a gravity dominated flow regime is found moving axially towards Plane A; the same is true for the representative film inlet boundary condition. Whilst a 5/95 percent split might be viable in achieving a more stable solution, there is an overall negligible difference in velocity observed with the DPM injection cases. Therefore, it is suspected that the same gravity dominated flow regime will still be found, since a 5/95 percent split will have a reduced amount of momentum exchange from droplets relative to the 10/90 split. This suggests that the lack of momentum exchange from droplets impinging on the thin film from the cage-edge does not influence the flow regime as originally expected. Due to the very limited information surrounding the oil exiting from the cage-edge, it is difficult to assess a more appropriate film inlet boundary condition. However, these results and the outcomes of Section 3, indicate that for future bearing chamber design it is not necessary to distribute oil from the cage-edge in order to prevent a dry-out region, although it may still be a necessary requirement for the heat management process over these surfaces. Overall, the originally proposed, representative film inlet boundary condition is therefore deemed the most suitable approach available. Future experimental work is recommended in providing more detailed measurements to support the development of a more suitable DPM inlet condition.

5. CONCLUSIONS

The two-way coupled ETFM-DPM solver, *sprayParcelFilmFoam*, has been successfully applied to a bearing chamber geometry, including the effects of both a film stripping and an edge separation criteria. Numerical studies are conducted over three different shaft speeds over two separate oil volume flow rates. A qualitative and quantitative analysis of the oil film is carried out and compared to the experimental data of Hee et al. [5].

Qualitatively results are found to be in excellent agreement with Hee et al. [5]. A shear dominated flow regime is observable at the Plane B location, however beyond this, due to the lack of experimental data, uncertainty arises as a gravity dominated flow regime is found under all shaft speeds investigated. Quantitatively, within the co- and counter-current regions, the results are able to accurately capture the axial variation of mean film thickness measurements. As the rotational shaft speed is increased, the reduction in film thickness follows a diminishing return with a minimum average film thicknesses of around 0.4mm over both flow rates studied that becomes independent of the shaft speed. An investigation into a more appropriate film inlet boundary condition was unsuccessful, resulting in a worse agreement with the experimental film thickness results of Hee et al. [5]. Through injecting DPM particles at the cage-edge location, the increase in velocity is not sufficient to over-come the gravity shear dominated flow regime at the edge, resulting in a more unstable film developing. Suggesting that the geometrical chamber configuration with a truncated shaft leads to a reduced shearing velocity and hence a reduced shearing force towards the front of the chamber, resulting in a gravity dominated flow regime.

Further experimental work is required to determine the flow regime state toward the front of the annulus, in order to determine whether a gravity dominated flow regime is indeed evident. Furthermore, a detailed breakdown of the oil exiting the cage-edge is also required to inform a more appropriate film inlet boundary condition. However, at present, the representative film inlet boundary condition is deemed appropriate for all future ETFM-DPM computational investigations. Computationally, work is now recommended in identifying and quantifying the droplets both stripped and separated from the film edge into the main chamber.

ACKNOWLEDGEMENTS

This project has received funding from the Clean Sky 2 Joint Undertaking under the European Union's Horizon 2020 research and innovation programme under grant agreement No 724625. The authors are grateful for the technical and financial support provided by Rolls-Royce. In addition, the authors acknowledge the use of the University of Nottingham High Performance Computing Facility as well as access to Athena at HPC Midlands+, which was funded by the EPSRC on grant EP/P020232/1.

REFERENCES

[1] A. Nicoli, R. Jefferson-loveday, and K. Simmons, "A New OpenFOAM Solver Capable of Modelling Oil Jet-Breakup And Subsequent Film Formation For Bearing Chamber Applications," *Proc. ASME Turbo Expo*, pp. 1–12, 2019.

[2] A. Glahn, M. Kurreck, M. Willmann, and S. Wittig, "Feasibility Study on Oil Droplet Flow Investigations Inside Aero Engine Bearing Chambers—PDPA Techniques in Combination With Numerical Approaches," *J. Eng. Gas Turbines Power*, vol. 118, no. 4, p. 749, 1996.

[3] P. Gorse, K. Dullenkopf, H.-J. Bauer, and S. Wittig, "An Experimental Study on Droplet Generation in Bearing Chambers Caused by Roller Bearings," *Proc. ASME Turbo Expo*, no. 43147, pp. 1681–1692, 2008.

[4] R. Santhosh, J. L. Hee, K. Simmons, G. Johnson, D. Hann, and M. Walsh, "Experimental Investigation of Oil Shedding From an Aero-Engine Ball Bearing at Moderate Speeds," *Proc. ASME Turbo Expo*, 2017.

[5] J. L. Hee, R. Santhosh, K. Simmons, G. Johnson, D. Hann, and M. Walsh, "Oil Film Thickness Measurements on Surfaces Close to an Aero-Engine Ball Bearing Using Optical Techniques," *Proc. ASME Turbo Expo*, 2017.

[6] A. Glahn and S. Wittig, "Two-Phase Air/Oil Flow in Aero Engine Bearing Chambers: Characterization of Oil Film Flows," *J. Eng. Gas Turbines Power*, vol. 118, p. 578, 1996.

[7] W. Kurz and H.-J. Bauer, "An Approach for Predicting the Flow Regime in an Aero Engine Bearing Chamber," *Proc. ASME Turbo Expo*, pp. 1–8, 2014.

[8] C. Eastwick, K. Huebner, B. Azzopardi, K. Simmons, C. Young, and R. Morrison, "Film Flow Around Bearing Chamber Support Structures," no. 47268. pp. 1267–1272, 2005.

[9] B. Chandra, K. Simmons, S. Pickering, and M. Tittel, "Factors Affecting Oil Removal From an Aeroengine Bearing Chamber," *Proc. ASME Turbo Expo*, pp. 219–228, 2011.

[10] B. Chandra, K. Simmons, S. Pickering, S. H. Collicott, and N. Wiedemann, "Study of Gas/Liquid Behavior Within an Aeroengine Bearing Chamber," *J. Eng. Gas Turbines Power*, vol. 135, no. 5, p. 051201, 2013.

[11] A. Nicoli, K. Johnson, and R. Jefferson-loveday, "Simulation Of A Simplified Aeroengine Bearing Using A Fully Coupled Two-Way Eulerian Thin Film/Discrete Phase Approach Part II: Droplet Behaviour In The Chamber," *J. Eng. Gas Turbines Power*, 2020.

[12] A. Bristot, H. P. Morvan, and K. A. Simmons, "Evaluation of a Volume of Fluid CFD Methodology for the Oil Film Thickness Estimation in an Aero-Engine Bearing Chamber," *Proc. ASME Turbo Expo*, no. 49712, pp. 1–11, 2016.

[13] A. Bristot, K. Simmons, and M. Klingsporn, "Effect of Turbulence Damping in VOF Simulation of an Aero-Engine Bearing Chamber," *Proc. ASME Turbo Expo*, pp. 1–10, 2017.

[14] J. Ashmore, A. E. Hosoi, and H. A. Stone, "The effect of surface tension on rimming flows in a partially filled rotating cylinder," *J. Fluid Mech.*, vol. 479, pp. 65–98, 2003.

[15] E. S. Benilov, V. N. Lapin, and S. B. G. O'Brien, "On rimming flows with shocks," *J. Eng. Math.*, pp. 49–62, 2012.

[16] M. Villegas-Diaz, H. Power, and D. S. Riley, "Analytical and numerical studies of the stability of thin-film rimming flow subject to surface shear," *J. Fluid Mech.*, vol. 541, pp. 317–344, 2005.

[17] E. D. Kay, S. Hibberd, and H. Power, "A depth-averaged model for non-isothermal thin-film rimming flow," *Int. J. Heat Mass Transf.*, vol. 70, pp. 1003–1015, 2014.

[18] B. Kakimpa, H. P. Morvan, and S. Hibberd, "Solution Strategies For Thin Film Rimming Flow Modelling," *Proc. ASME Turbo Expo*, 2015.

[19] B. Kakimpa, H. Morvan, and S. Hibberd, "The Depth-Averaged Numerical Simulation of Laminar Thin-Film Flows With Capillary Waves," *J. Eng. Gas Turbines Power*, vol. 138, 2016.

[20] B. Kakimpa, H. P. Morvan, and S. Hibberd, "Thin-Film Flow Over a Rotating Plate: An Assessment of the Suitability of VOF and Eulerian Thin-Film Methods for the Numerical Simulation of Isothermal Thin-Film Flows," *Proc. ASME Turbo Expo*, 2015.

[21] B. Kakimpa, H. P. Morvan, and S. Hibberd, "The numerical simulation of multi-scale oil films using coupled VOF and Eulerian thin-film models," *Proc. ASME Turbo Expo*, 2016.

[22] K. Singh, M. Sharabi, S. Ambrose, C. Eastwick, and R. Jefferson-loveday, "Prediction of Film Thickness of an Aero-Engine Bearing Chamber Using Coupled VOF and Thin Film Model," *Proc. ASME Turbo Expo*, 2019.

[23] K. Singh, M. Sharabi, S. Ambrose, C. Eastwick, R. Jefferson-loveday, and J. Cao, "Assessment of an Enhanced Thin Film Model to Capture Wetting and Drying," *Proc. ASME Turbo Expo*, 2019.

[24] A. A. Adeniyi, H. P. Morvan, and K. A. Simmons, "A Multiphase Computational Study of Oil-Air Flow Within the Bearing Sector of Aeroengines," *Proc. ASME Turbo Expo*, 2015.

[25] A. Nicoli, "Development and Application of a Fully Coupled Eulerian Thin Film/Discrete Phase Approach to a Simplified Aeroengine Bearing Chamber," PhD Thesis, University of Nottingham, 2020.

[26] K. V. Meredith, A. Heather, J. de Vries, and Y. Xin, "A numerical model for partially-wetted flow of thin liquid films," in *WIT Transactions on Engineering Sciences*, 2011.

[27] P. Gorse, K. Willenborg, S. Busam, J. Ebner, K. Dullenkopf, and S. Wittig, "3D-LDA Measurements in an Aero-Engine Bearing Chamber," *Proc. ASME Turbo Expo*, no. 36886, pp. 257–265, 2003.